JACS Au
AN OPEN ACCESS JOURNAL OF THE AMERICAN CHEMICAL SOCIETY

pubs.acs.org/jacsau
Article

High-Throughput Screening of Sulfur Reduction Reaction Catalysts Utilizing Electronic Fingerprint Similarity

Hongwei Shou, Quan Zhou, Shiqiang Wei, Hengjie Liu, Haifeng Lv,* Xiaojun Wu,* and Li Song*

Cite This: JACS Au 2024, 4, 930−939

Read Online

ACCESS | Metrics & More | Article Recommendations | Supporting Information

ABSTRACT: The catalytic performance is determined by the electronic structure near the Fermi level. This study presents an effective and simple screening descriptor, i.e., the one-dimensional density of states (1D-DOS) fingerprint similarity, to identify potential catalysts for the sulfur reduction reaction (SRR) in lithium−sulfur batteries. The Δ1D-DOS in relation to the benchmark W_2CS_2 was calculated. This method effectively distinguishes and identifies 30 potential candidates for the SRR from 420 types of MXenes. Further analysis of the Gibbs free energy profiles reveals that MXene candidates exhibit promising thermodynamic properties for SRR, with the protocol achieving an accuracy rate exceeding 93%. Based on the crystal orbital Hamilton population (COHP) and differential charge analysis, it is confirmed that the Δ1D-DOS could effectively differentiate the interaction between MXenes and lithium polysulfide (LiPS) intermediates. This study underscores the importance of the electronic fingerprint in catalytic performance and thus may pave a new way for future high-throughput material screening for energy storage applications.

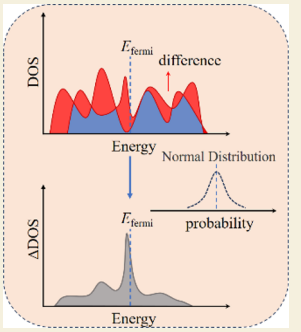

KEYWORDS: *MXene, sulfur reduction reaction, DFT, 1D-DOS, fingerprint similarity, high-throughput screening*

INTRODUCTION

In recent years, a variety of intrinsic electronic descriptors have been successfully used to predict the reaction barriers of materials through first-principles calculations, high-throughput screening, and machine learning.[1−3] For example, by calculating the integrated crystal orbital Hamilton population (ICOHP), it has been found that an appropriate M-N bond strength is crucial for nitrogen reduction reaction (NRR) catalysts.[4] The hybridization state of d-p orbitals between single atom catalysts (SACs) and sulfides can serve as a reliable descriptor for screening high-performance SACs for lithium−sulfur batteries.[5] In addition, the scaling relationship between Δ(d-p) and the redox potential of S_6^{2-}/S^{2-} clearly shows the important role played by the p-band position originating from nonmetal anions in influencing interfacial electron transfer dynamics in Li−S chemistry.[6] By considering the p-band center of MXene surface functional groups and the electronegativity of the subsurface metal, a scaling relationship between ΔG_{min} and the descriptor was revealed.[7] Huang et al. used machine learning to reveal a strong correlation between the decomposition barrier of Na_2S and the number of outermost electrons of the metal element.[8] Based on the valence electrons and electronegativity of MXene surface and subsurface atoms, several potential MXene catalysts with good C−N coupling performance were discovered.[9]

All the above-mentioned studies highlight the pivotal role of electronic structure in catalytic reactions,[10] indicating the fingerprint effect of electronic structure.[11,12] The zero-dimensional (0D) d-band center, p-band center, and their derived descriptors are merely a portion of the one-dimensional density of state (1D-DOS) and reflect limited information about the materials' electronic fingerprint,[5,13−15] as the bandwidth, occupied states, and unoccupied states also constitute an integral part of the electronic properties.[16] The 1D-DOS can display the distribution of electrons in the entire energy space, and similar electronic fingerprints often exhibit similar physicochemical properties toward intermediates in catalytic reactions.[17] For example, RhAg alloy, because of its electronic hybridization, has a similar DOS to pure Pd and thus also possesses hydrogen storage properties.[18,19] This method has also been successfully used to screen bimetallic H_2O_2 catalysts, revealing four catalysts with comparable performance to Pd, and an excellent, previously unreported $Ni_{61}Pt_{39}$ catalyst for direct H_2O_2 synthesis.[17] DOS fingerprints are a potent tool in differentiating between metals, semiconductors, topological insulators, piezoelectrics, and superconductors.[11] Even if the materials have different structures, they can still be grouped into a cluster based on their DOS fingerprint similarity.[12] DOS can also be implemented to accurately predict catalytic properties, such as adsorption energies.[10,20,21]

This screening process, which does not involve the optimization of intermediate structures, is particularly suitable for complex catalytic reactions with numerous transforming

Received: November 14, 2023
Revised: January 3, 2024
Accepted: January 9, 2024
Published: February 27, 2024

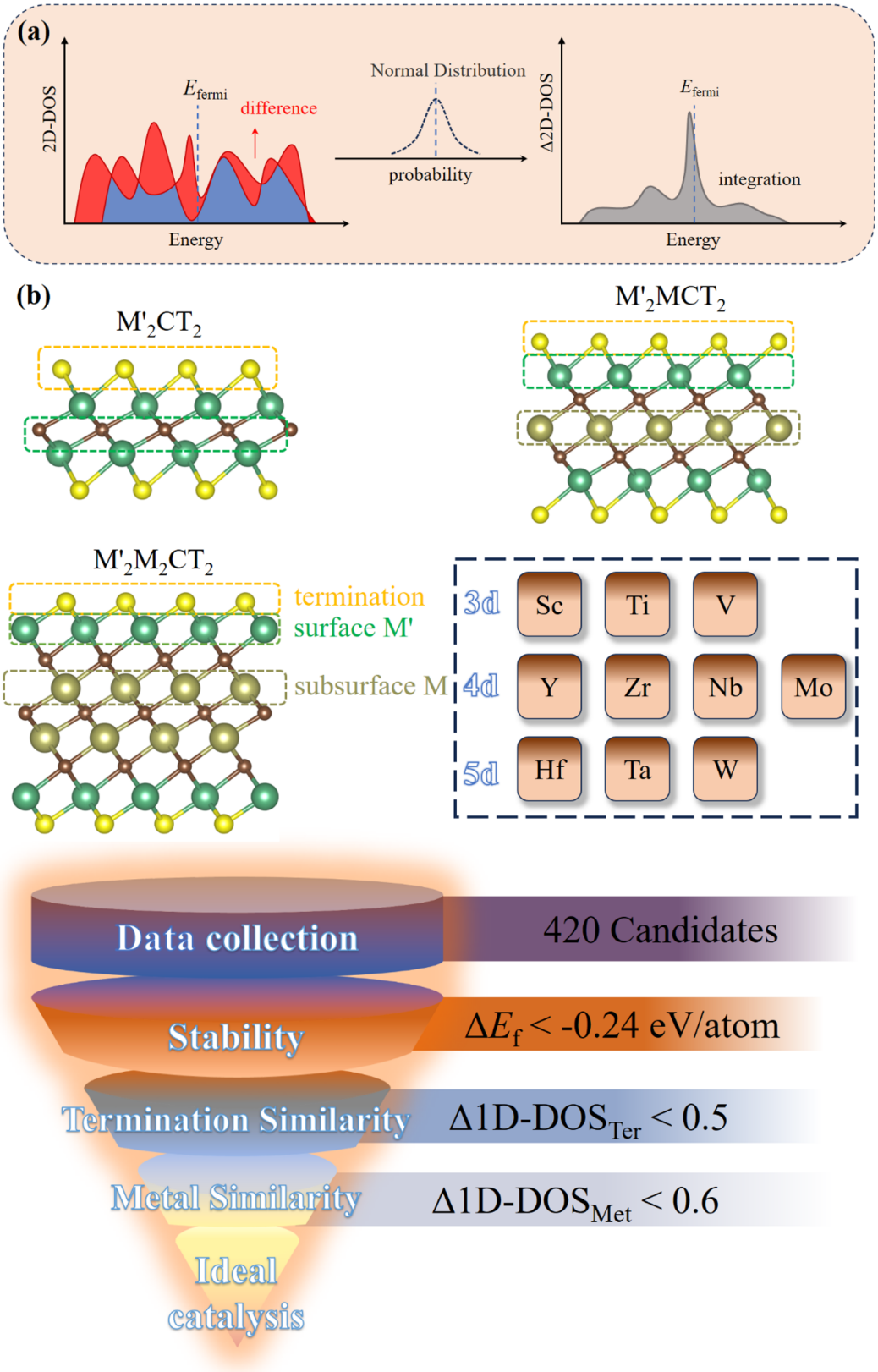

Figure 1. (a) Schematic representation of the calculation of the 1D-DOS fingerprint similarity (Δ1D-DOS). (b) High-throughput screening protocol for the discovery of MXenes.

intermediates, such as the sulfur reduction reaction (SRR).[22] Li−S batteries, with their extremely high theoretical capacity density of 2567 Wh/kg, are one of the most promising next-generation energy storage devices.[7,23] However, the practical application of these batteries is hampered by the shuttle effect of lithium polysulfides (LiPS) and the slow kinetics of multielectron sulfur reduction reactions.[23,24] MXene, with its tunable surface groups and compositions, offers strong

https://doi.org/10.1021/jacsau.3c00710
JACS Au 2024, 4, 930−939

chemical adsorption for polysulfides and rapid catalytic kinetics, making it an attractive option for high-performance Li−S batteries.[25−27] However, because of the highly tunable surface functional groups and inherent metal types of MXene,[28,29] its structural vector space tends toward infinity, making it challenging to screen MXene suitable for SRR.

In this contribution, W_2CS_2, identified as a potential cathodic catalyst for SRR,[7] was used as a benchmark MXene. Based on the similarity of 1D-DOS of the surface termination and surface metal M, 420 types of MXenes were screened, and 30 ideal MXene catalysts for SRR were identified. By comparing MXenes with large similarity in 1D-DOS, it has been found that a similar 2D-DOS fingerprint leads to similar adsorption effects on intermediates. The distribution of the 1D-DOS fingerprint at different energies significantly affects the adsorption behavior of intermediates. For instance, MXenes with small Δ1D-DOS show strong adsorption for LiPS intermediates and vice versa. In our study, detailed Gibbs free energy diagrams for the sulfur reduction reaction (SRR) were meticulously calculated. It was found that 27 out of the total identified catalysts could significantly enhance the efficiency of Li−S batteries by promoting the transformation of the LiPS intermediates. Impressively, an accuracy rate of up to 93% was achieved through this refined screening process, underscoring the robustness and effectiveness of our method. A volcano plot was constructed, revealing that the best activity is exhibited by $M'_2MC_2O_2$, whereas the lowest activity is shown by M_2CO_2, primarily due to the favorable transformation of LiS by $M'_2MC_2O_2$. For the SRR, a voltage of up to 1.64 V can be provided by $W_2ZrC_2O_2$. A relatively simple high-throughput process using 1D-DOS fingerprint similarity to bypass adsorption intermediates for screening MXene suitable for SRR was proposed. This study underscores the importance of the electronic fingerprint in catalytic performance.

COMPUTATIONAL METHOD

DFT Calculations

All DFT[30] calculations were performed using the Vienna Ab initio Simulation Package (VASP)[31] within the project augmented wave method (PAW).[32] Exchange and correlation energy is performed by the Perdew−Burke−Ernzerhof (PBE) version of the generalized gradient approximation (GGA).[33]. The Brillouin zone is sampled using 7 × 4 × 1 based on the Monkhorst−Pack k-point mesh during geometric optimization, with the DFT-D3 semiempirical correction method for van der Waals interactions.[34,35] Self-consistent field (SCF) calculations were performed with an energy and force convergence criterion of 1×10^{-8} eV and 0.01 eV·Å^{-1}, respectively. The cutoff energy was set as 450 eV. A vacuum region in the direction perpendicular to the surface was set at least 15 Å to avoid the interaction between images. The electronic structure of MXene was calculated by using a K-point density of 22 × 12 × 1. All electronic structures have been depicted in the Supporting Information.

The reaction elementary steps of the SRR are as follows:

$$^*S_8 + 2Li^+ + 2e^- \rightarrow {}^*Li_2S_8$$

$$^* + 3{}^*Li_2S_8 + 2Li^+ + 2e^- \rightarrow 4{}^*Li_2S_6$$

$$^* + 2{}^*Li_2S_6 + 2Li^+ + 2e^- \rightarrow 3{}^*Li_2S_4$$

$$^* + {}^*Li_2S_4 + 2Li^+ + 2e^- \rightarrow 2{}^*Li_2S_2$$

$$^* + {}^*Li_2S_2 \rightarrow 2{}^*LiS$$

$$^*LiS + Li^+ + e \rightarrow {}^*LiS$$

MXene Databases

In this study, six classes of MXenes were considered, inclusive of 20 monometallic M_2CT_2 and 400 ordered bimetallic $M'_2MC_2T_2$ and $M'_2M_2C_3T_2$, which total 420 MXenes (where M', M = Sc, Ti, V, Y, Zr, Nb, Mo, Hf, Ta, and W and T = O and S termination). As shown in Figure 1b, for ordered bimetallic $M'_2MC_2T_2$ and $M'_2M_2C_3T_2$, M' denotes the surface metal, and M represents the subsurface metal. However, it is noteworthy that the determination of which metal would render the MXene more stable when it serves as the surface metal was not considered in our endeavor to ascertain whether 1D-DOS fingerprint similarity can be effectively utilized for material screening, although we know that the sandwich structure may be energetically favored when the surface layer is Ti, V, or Mo.[9,36,37]

AIMD Simulations

In the ab initio molecular dynamics (AIMD) simulations, a time step of 2 fs was employed. These simulations were restricted to the gamma point within the Brillouin zone, disregarding any symmetry considerations. The system was simulated at 1000 K with a Nosé−Hoover thermostat for 12 ps.

1D-DOS Fingerprint Similarity

A difference formula was defined to quantitatively compare the similarity between two 1D-DOS:

$$\Delta 1\mathrm{DDOS}_i = \left[\int_{-\infty}^{+\infty} \left(1\mathrm{DDOS}(E)_i - 1\mathrm{DDOS}(E)_{W_2CS_2}\right)^2 * N(E, \mu, \sigma^2)\right]^{1/2} \quad (1)$$

$$N(E, \mu, \sigma^2) = \frac{1}{\sigma\sqrt{2\pi}} \exp^{-(E-\mu)^2/2\sigma^2} \quad (2)$$

Here, $\Delta\mathrm{DOS}_i$ represents the difference between the two 1D-DOS. A larger value indicates a greater difference between the two electronic fingerprints near the Fermi surface. 1D $\mathrm{DOS}(E)_i$ and 1D $\mathrm{DOS}(E)_{W_2CS_2}$ represent the calculated 1D-DOS of MXene and the W_2CS_2 benchmark, respectively. $N(E, \mu,$ and $\sigma^2)$ is a normal distribution that signifies the weighted processing of 1D-DOS in different regions of the MXene. According to the frontier molecular orbital theory,[38] interactions between the MXene and adsorbed intermediates are primarily determined by electrons near the Fermi level;[39] thus, $\mu = E_F$ and $\sigma = 7$ in the formula. The range from −7 to 7 eV already encompasses most features of the 1D-DOS spectrum, adequately characterizing different forms of interactions during the reaction process. Moreover, the center of the 0D d-band and p-band also lies within this range.[6−8] Because of the strong interaction between the adsorbed species and the sp-band DOS of MXene, both the d-band and sp-band must be considered.[17] Therefore, TDOS is used to calculate the 1D-DOS fingerprint similarity.

https://doi.org/10.1021/jacsau.3c00710
JACS Au 2024, 4, 930−939

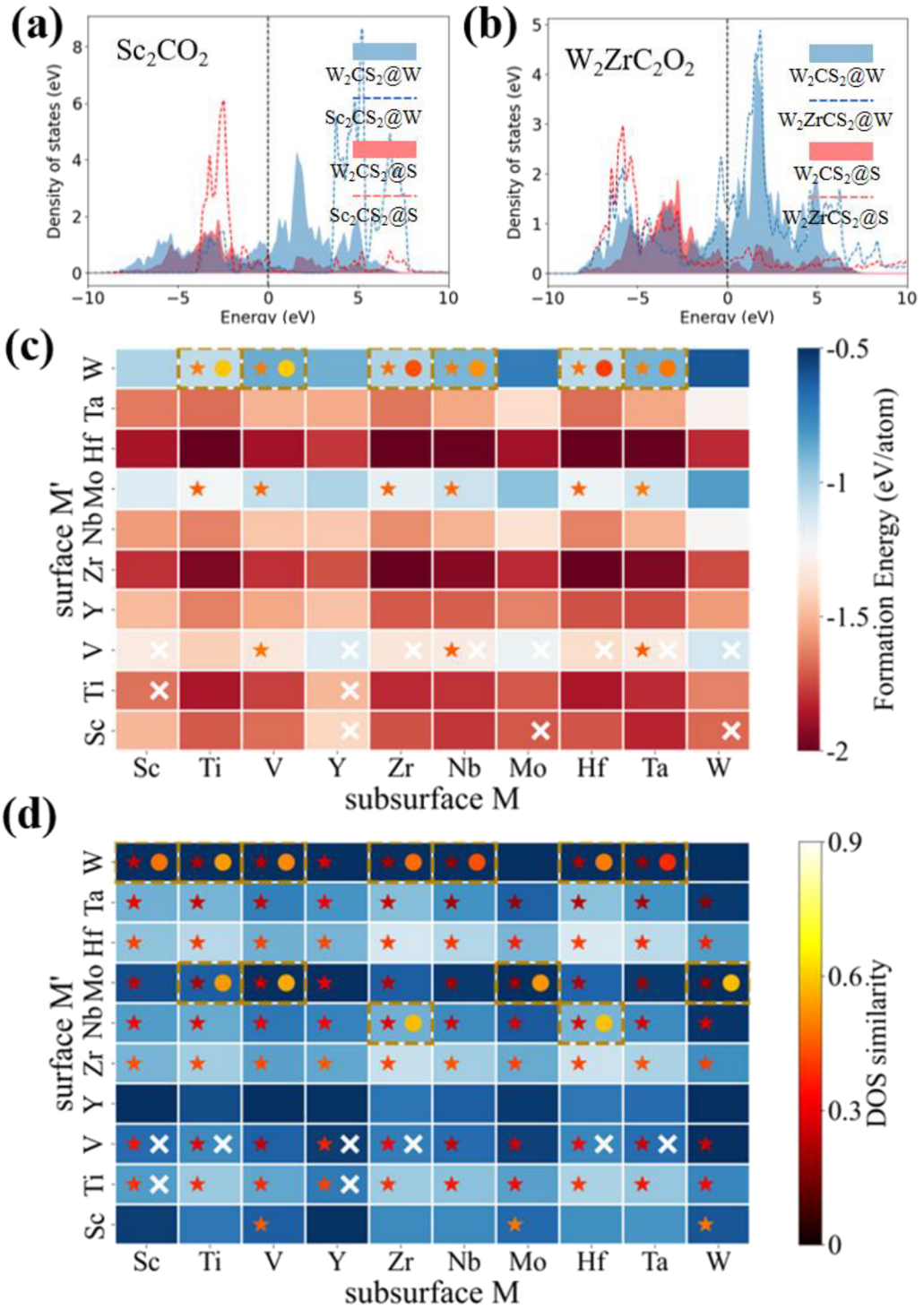

Figure 2. (a, b) Comparison of the 1D-DOS spectra for Sc_2CO_2, $W_2ZrC_2O_2$, and W_2CS_2. The blue and red shadows represent the density of states for the surface metal W and termination layer S of W_2CS_2, respectively. The blue and red dashed lines represent the density of states for the surface metal and termination layer of Sc_2CO_2 and $W_2ZrC_2O_2$, respectively. (c, d) Screening results for $M'_2MC_2O_2$ and $M'_2MC_2S_2$. The color of the heatmap represents the formation energy. The stars on the left represent termination similarity, and the circles on the right represent metal similarity, with the color representing the degree of difference. The white crosses represent a termination or metal similarity greater than 1.2.

RESULTS AND DISCUSSION

High-Throughput Screening Protocol

Figure 1b presents a schematic of the high-throughput protocol. Initially, 420 monometallic and ordered bimetallic sandwich MXenes were constructed. Subsequently, their enthalpy of formation was calculated. However, because of the presence of functional groups on the MXene surface, the enthalpy of formation for functional MXenes is relatively small.[40−42] To increase the likelihood of experimental synthesis, we set a stringent standard for the enthalpy of formation at less than −0.24 eV/atom. Heatmaps of the enthalpy of formation are depicted in Figure 2c,d and Figures S1−S4, with the corresponding data listed in Tables S1−S6. It

https://doi.org/10.1021/jacsau.3c00710
JACS Au 2024, 4, 930−939

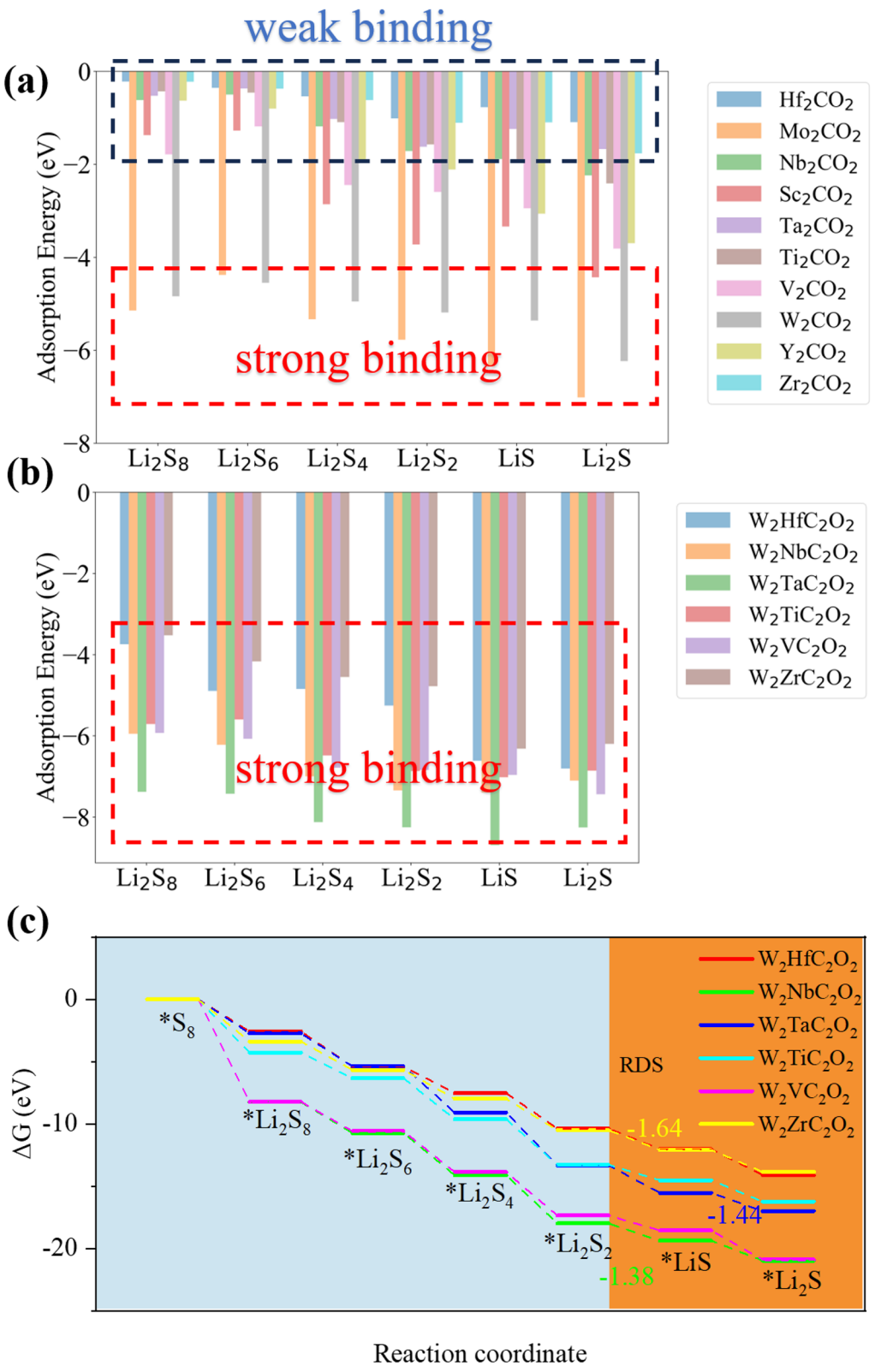

Figure 3. (a, b) Adsorption energy of LiPS on M_2CO_2 and $M'_2MC_2O_2$. (c) Gibbs free energy profiles of $M'_2MC_2O_2$ for the SRR process.

was found that the majority of MXenes have a small enthalpy of formation, with only $W_3C_2S_2$, $W_2MoC_2S_2$, $W_2Mo_2C_3S_2$, and $W_4C_3S_2$ having larger values of −0.04, −1.15, −0.13, and 0.05 eV/atom, respectively.[36] This suggests that most MXenes can be synthesized experimentally. However, it is worth noting that the enthalpy of formation for M_2CO_2, $M'_2MC_2O_2$, and $M'_2M_2C_3O_2$ MXenes is less than that for the corresponding S-termination MXenes,[43] indicating that it is easier to produce O-termination MXenes experimentally. Therefore, this paper mainly discusses the SRR of the O-termination MXenes. Next, the DOSs of the termination layer and surface metal were extracted, and Δ1DDOS was calculated based on Figure 1a

https://doi.org/10.1021/jacsau.3c00710
JACS Au 2024, 4, 930−939

and eq 2. The thresholds were set at 0.5 and 0.6, respectively. The lower threshold for termination is due to the fact that the surface is the main site for chemical reactions, hence necessitating a higher screening requirement. The results of Δ1DDOS were superimposed on the enthalpy images, as depicted in Figure 2c,d and Figures S1−S4. The electrons near the Fermi level of W_2CS_2 are primarily provided by the metal W, with a small contribution from nonmetal S (Figure 2a,b). W and S exhibit strong d-p orbital hybridization within the −4 to −3 eV range. W and S have numerous vacant orbitals 1−2 eV above the Fermi level. For monometallic M_2CO_2, only Mo_2CO_2 meets the criteria due to the considerable Δ1DDOS of the termination layer (Figure S5). Sc_2CO_2, Ti_2CO_2, and Y_2CO_2 have Δ1DDOS values exceeding 1.2 (Figure 1a, Figure S5), indicating a stark difference in electronic fingerprint near the Fermi level compared with W_2CS_2. This is primarily because Sc_2CO_2 has a significant band gap in the 0−3 eV range, making it a wide band gap semiconductor.[44,45] A similar scenario is observed for Y_2CO_2.[46] A few alternatives exist in $M'_2MC_2O_2$, such as $W_2TiC_2O_2$, $W_2VC_2O_2$, $W_2ZrC_2O_2$, $W_2NbC_2O_2$, $W_2HfC_2O_2$, and $W_2TaC_2O_2$ (Figure 2c, Figures S6−S15), all of which are W-based MXenes. Regrettably, whereas Mo-based $M'_2MC_2O_2$ has a smaller Δ1D-DOS for termination, the larger Δ1D-DOS for the surface-metal Mo makes it unsuitable for selection. A large number of $M'_2M_2C_3O_2$ MXenes with Δ1D-DOS greater than 1.2 exist, suggesting that M_4C_3 type MXenes (except $Mo_2V_2C_3O_2$) may not be suitable for SRRs (Figure S2). The situation for M_2CS_2 and M_2CO_2 is similar, with only Mo_2CS_2 as a candidate, indicating the similar electronic fingerprint of Mo and W (Figure S3). Therefore, Mo-based MXenes such as $Mo_2TiC_2S_2$, $Mo_2VC_2S_2$, $Mo_3C_2S_2$, and $Mo_2WC_2S_2$ were identified in $M'_2MC_2S_2$. A similar scenario is observed for $M'_2M_2C_3S_2$, which contains a large number of W-based and Mo-based MXenes. Finally, 30 candidates were obtained, indicated by the yellow boxes in the figure. Overall, this simple high-throughput 1D-DOS calculation and numerical processing method, which does not require the optimization of the adsorption geometry of intermediates, allows us to obtain potential MXenes for SRR in just a few hours.

Adsorption Characteristic Analysis of LiPS Intermediates

To ascertain whether the Coulombic interactions between the MXenes screened out through this high-throughput calculation of Δ1D-DOS and the adsorbed species are similar, the adsorption energy between 30 candidate MXenes and LiPS intermediates was calculated. Additionally, to enhance contrast, M_2CT_2 (M = Sc, Ti, V, Y, Zr, Nb, Hf, Ta; T = O, S), MXenes with larger Δ1D-DOS values were also detailedly computed for comparison. From Figure 3a, it can be observed that M_2CO_2's adsorption of LiPS intermediates is distinctly divided into two categories, one being Mo_2CO_2 and W_2CO_2 with smaller Δ1D-DOS values and the other being Hf_2CO_2, Sc_2CO_2, etc., with larger Δ1D-DOS values. The former exhibits strong binding with LiPS intermediates, with an adsorption energy ranging from −4.1 to −7 eV. The latter exhibits weak binding with LiPS, with most of the adsorption energy ranging from 0 to −2 eV. The smaller adsorption energy cannot suppress the shuttle effect of polysulfides, leading to the rapid deactivation of Li−S batteries. The six selected W-based $W_2MC_2O_2$ (M = Hf, Nb, Ta, Ti, V, Zr) and $Mo_2V_2C_3O_2$ also possess similar strong binding with W_2CS_2 (Figure 3b and Figure S47). Furthermore, M_2CS_2 MXenes can also be clearly classified into two categories based on Δ1D-DOS (Figure S48). Unfortunately, it has been found that in $M'_2MC_2S_2$ MXenes, $Nb_2HfC_2S_2$, and $Nb_2ZrC_2S_2$ are exceptions (Figure S49). Even so, the efficiency of screening SRR catalysts using a 1D-DOS fingerprint similarity is astonishing.

Gibbs Free Energy Profile of SRR

Subsequently, the Gibbs free energy profile of the SRR for the aforementioned MXenes was calculated to confirm their SRR potential. The calculation path was adopted as $*S_8 \rightarrow *Li_2S_8 \rightarrow *Li_2S_6 \rightarrow *Li_2S_4 \rightarrow *Li_2S_2 \rightarrow *LiS \rightarrow *Li_2S$. Figure S51 shows that both Mo_2CO_2 and W_2CO_2 can be used for SRR, with the rate-determining step being the transformation of the Li_2S_2 intermediate into a LiS intermediate with activities of −0.42 and −1.11 eV, respectively. By removing the intermediate layer of Mo_2SnC, a functionalized Mo_2C−CNT composite cathode material was prepared as a good conductive anchoring matrix for sulfur in Li−S batteries, with a reversible capacity of approximately 925 mAh/g.[27] The electrode of S@Mo_2CTx prepared by Yang and his colleagues also demonstrated rapid charging and lithium-ion transport capabilities.[47] Another category of M_2CO_2 (M = Sc, Ti, V, Y, Zr, Nb, Hf, and Ta) is not conducive to the transformation of LiPS intermediates (Figure S52). The rate-determining step also includes the dissociation and transformation of Li_2S_2. Hf_2CO_2 has an overpotential as high as 2.08 eV, making it almost impossible to utilize for the sulfur reduction reaction (SRR), and there are also no experimental reports of its use. V_2CO_2 has an overpotential of 0.7 eV, similar to literature reports.[48,49] The Gibbs free energy diagram further clarifies that M_2CO_2 can be divided into two categories. The former can be used for the transformation of LiPS intermediates, but the latter cannot (Figures S51−S52). The screened W-based $M'_2MC_2O_2$ can all promote the transformation of LiPS intermediates (Figure 3c). The activity of $W_2ZrC_2O_2$ is as high as 1.64 eV. The rate-determining step for most $M'_2MC_2O_2$ is also the dissociation and conversion of Li_2S_2.[50] Only $W_2TiC_2O_2$ differs, where the conversion of the LiS intermediate to Li_2S is the rate-determining step, with an activity of 1.44 eV.[51] The activity of $Mo_2V_2C_3O_2$ is 1.25 eV. M_2CS_2 can also be divided into two categories based on Δ1D-DOS. Unfortunately, in the SRR process of $Nb_2HfC_2S_2$ and $Nb_2ZrC_2S_2$, there is one reaction step that is endothermic, with barriers of 0.32 and 0.25 eV, respectively. However, these barriers are much smaller than those of other MXenes with larger Δ1D-DOS. Using $\Delta G(*Li_2S)$ and $\Delta G(*LiS)$, we constructed a volcano plot for the SRR of MXene. For M_2CO_2 type MXene with a larger Δ1D-DOS (shown as area 1 in the figure), the main reason limiting its activity is the larger $\Delta G(*LiS)$. As $\Delta G(*LiS)$ decreases, the activity of the MXene also increases, with most materials located in this transition area. The materials in area 2, namely, $W_2NbC_2O_2$, $W_2ZrC_2O_2$, and $W_2TaC_2O_2$, exhibit the best activity. Furthermore, the decomposition kinetic barrier of Li_2S is also crucial for the performance of Li−S batteries. The decomposition barrier of Li_2S was studied in Figure S58. As indicated, the barriers for $W_2TaC_2O_2$, $WNb_2C_2O_2$, and $W_2ZrC_2O_2$ are 0.66 0.55, and 0.78 eV, respectively. The decomposition barrier for pure Li_2S is calculated to be 3.64 eV.[52] The optimal MXenes can effectively reduce the decomposition barrier of Li_2S. Overall, Δ1D-DOS is a very effective high-throughput protocol for material screening, achieving an accuracy rate as high as 93% in this study for the identification of MXene for SRR catalysts.

https://doi.org/10.1021/jacsau.3c00710
JACS Au 2024, 4, 930−939

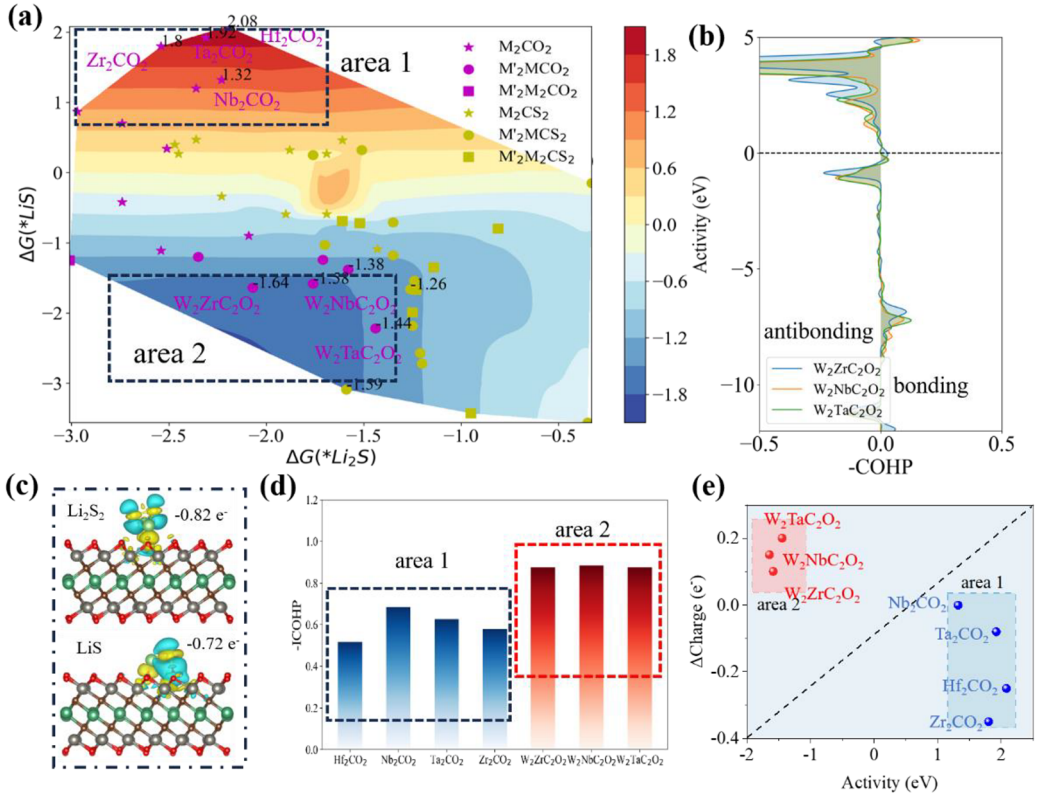

Figure 4. (a) Two-dimensional (quasi) activity volcano plot for the SRR process, shown with two independent descriptors: $\Delta G(*Li_2S)$ and $\Delta G(*LiS)$. (b) Crystal orbital Hamilton populations (COHPs) for $W_2ZrC_2O_2$, $W_2NbC_2O_2$, and $W_2TaC_2O_2$. (c) Charge differential map of Li_2S_2 and LiS on $W_2ZrC_2O_2$. The isosurface is −0.002 $e^-/Å^3$. Yellow shading represents a gain of electrons; light blue represents a loss of electrons. (d) ICOHP for MXenes in area 1 and area 2. (e) Relationship between Δcharge and activity.

Electronic Structure Analysis

To demonstrate that the 1D-DOS fingerprint leads to varying interactions with LiPS intermediates, we calculated the crystal orbital Hamilton populations (COHPs) for MXenes in areas 1 and 2 with LiS intermediates. As illustrated in Figure S59, the bonding states of Hf_2CO_2, Nb_2CO_2, Ta_2CO_2, and Zr_2CO_2 with LiS intermediates are all located in the region from −8 to −6 eV. Meanwhile, the bonding and antibonding states of $W_2ZrC_2O_2$, $W_2NbC_2O_2$, and $W_2TaC_2O_2$ are respectively located in the ranges of −8 to −6 eV and −1.5 to 0 eV (Figure 4b). By integration of the COHP below the Fermi level, the contribution to bonding between adjacent atoms can be estimated, thereby quantifying the bonding strength. Our research shows that the ICOHP between MXenes in area 1 and LiS intermediates is less than 0.75 eV, whereas those in area 2 are greater than 0.85 eV, indicating stronger bonding between MXenes in area 2 and LiS intermediates. This is consistent with our previous analysis of the adsorption energy. Therefore, based on 1D-DOS fingerprint similarity, we can indeed differentiate the interactions of MXenes with LiPS intermediates, thus screening out MXenes with strong interactions.

In addition, considering that the rate-determining step for most MXenes is the transformation from Li_2S_2 to LiS, we calculated the differential charge between Li_2S_2, LiS, and MXenes. From Figure S67, it can be seen that MXenes in area 2 have a strong charge transfer with Li_2S_2, all above 0.82 e^-. Interestingly, we calculated the difference in electron transfer numbers between Li_2S_2 and LiS, and we found that the difference in electron transfer numbers of MXenes in area 2 is all greater than that in area 1 (Figure 4e), suggesting that such electron transfer may be beneficial for the transformation of Li_2S_2 to LiS intermediates.

The Stability and Synthesis of the Ideal MXenes

The stability of the optimal MXenes was investigated by calculating the phonon dispersions of $W_2TaC_2O_2$, $W_2NbC_2O_2$, and $W_2ZrC_2O_2$. The studies indicate that the structures are stable. Furthermore, the AIMD simulations were conducted at a high temperature of 1000 K for 12 ps with a time step of 2 fs. As shown in Figure S69, the energy and temperature of the three materials oscillate in near equilibrium states. Moreover, even under a high temperature of 1000 K, they maintain a relatively good crystalline structure. Based on the phonon dispersions and AIMD results, the $W_2TaC_2O_2$, $W_2NbC_2O_2$, and $W_2ZrC_2O_2$ MXenes are confirmed to be stable.

W-based MXenes have been theoretically proven to be stable and have already been used in batteries, in catalysis, and even in the biomedical field.[53] Ordered vacancies in 2D $W_{1.33}C$ i-MXene have been obtained through the etching of ordered in-plane $(W_{2/3}Y_{1/3})_2AlC$ or $(W_{2/3}Sc_{1/3})_2AlC$.[54,55] Cui et al. synthesized new in-plane ordered, rare-earth-containing $(W_{2/3}R_{1/3})_2AlC$ (R = Gd, Tb, Dy, Ho, Er, Tm, and Lu) i-MAX phases and successfully exfoliated them.[56] It is possible to obtain the ideal MXenes screened out through a top-down etching approach of i-MAX phases containing W and Ta. Additionally, a bottom-up chemical vapor deposition (CVD) method has also been used to synthesize a large number of unconventional MXenes.[57] Therefore, this method could also be a candidate for synthesizing $W_2TaC_2O_2$, $W_2NbC_2O_2$, and $W_2ZrC_2O_2$ MXenes. Overall, this work has rapidly screened

https://doi.org/10.1021/jacsau.3c00710
JACS Au 2024, 4, 930−939

catalysts favorable for the SRR from 420 types of MXenes using 1D-DOS fingerprint similarity screening, greatly reducing experimental and time costs.

CONCLUSIONS

In conclusion, as the catalytic properties are determined by the electronic structure, our study introduces a high-throughput protocol that utilizes 1D-DOS fingerprint similarity to screen catalytic materials, bypassing the traditional, complex geometric optimization of intermediates and catalytic mechanism calculations. Using the sulfur reduction reaction (SRR) as a test case, we validated the accuracy of this protocol. Results show that by calculating the Δ1D-DOS relative to the benchmark W_2CS_2, we can effectively distinguish MXenes conducive to the SRR and identify 30 potential candidates. MXenes with small 1D-DOS fingerprint similarity tend to exhibit similar adsorption behaviors with lithium polysulfide (LiPS) intermediates and categorize materials into strong and weak adsorptions for LiPS.

Further analysis of the Gibbs free energy profiles revealed that most of these selected MXenes exhibit promising thermodynamic properties suitable for SRR, with an accuracy rate exceeding 93%. The rate-determining step for most of these MXenes was identical: the transformation of the Li_2S_2 intermediate into LiS. The activity of $W_2ZrC_2O_2$ is as high as 1.64 eV. Moreover, through the analysis of the crystal orbital Hamilton population (COHP) and differential charge, it was substantiated that the 1D-DOS similarity can effectively differentiate the interaction between MXenes and LiPS intermediates.

All in all, this high-throughput protocol based on the 1D-DOS fingerprint similarity provides a rapid and accurate approach for the identification of potential SRR catalysts. The findings of this study underscore the importance of the electronic fingerprint in the catalytic performance of materials, offering invaluable insights and guidance for the future design and selection of catalyst materials for energy storage applications.

ASSOCIATED CONTENT

Supporting Information

The Supporting Information is available free of charge at https://pubs.acs.org/doi/10.1021/jacsau.3c00710.

Screening results for M_2CO_2, $M'_2M_2C_3O_2$ M_2CS_2, and $M'_2M_2C_3S_2$ MXene; comparison of the density of states for M_2CO_2, $M'_2MC_2O_2$, $M'_2M_2C_3O_2$, M_2CS_2, $M'_2MC_2S_2$,and $M'_2M_2C_3S_2$; adsorption energy of LiPS on different MXenes; Gibbs free energy profiles of different MXenes; the detailed Gibbs free energy for the conversion of Li_2S_2 to Li_2S; energy profiles for the decomposition of Li_2S cluster on $W_2TaC_2O_2$, $W_2NbC_2O_2$ and $W_2ZrC_2O_2$; crystal orbital Hamilton populations (COHPs) for Hf_2CO_2, Nb_2CO_2, Ta_2CO_2, and Zr_2CO_2; Bader charge for M_2CO_2, $M'_2MC_2O_2$, $M'_2M_2C_3O_2$, M_2CS_2, $M'_2MC_2S_2$, and $M'_2M_2C_3S_2$; charge differential map for Li_2S_2 and LiS on Hf_2CO_2, Nb_2CO_2, Ta_2CO_2, and Zr_2CO_2 in area 1; charge differential map for Li_2S_2 and LiS on $W_2NbC_2O_2$, $W_2TaC_2O_2$, and $W_2HfC_2O_2$ in area 2; the phonon dispersions, the variations of temperature and energy with time during AIMD simulations, and the top and side views of the snapshots of atomic configurations after AIMD for $W_2TaC_2O_2$, $W_2NbC_2O_2$, and $W_2ZrC_2O_2$; the formation energy of M_2CO_2, $M'_2MC_2O_2$, $M'_2M_2C_3O_2$, M_2CS_2, $M'_2MC_2S_2$, and $M'_2M_2C_3S_2$; the fingerprint similarity for termination of M_2CO_2, $M'_2MC_2O_2$, $M'_2M_2C_3O_2$, M_2CS_2, $M'_2MC_2S_2$, and $M'_2M_2C_3S_2$; the formation energy of M_2CO_2, $M'_2MC_2O_2$, $M'_2M_2C_3O_2$, M_2CS_2, $M'_2MC_2S_2$, and $M'_2M_2C_3S_2$; and the fingerprint similarity for metal of M_2CO_2, $M'_2MC_2O_2$, $M'_2M_2C_3O_2$, M_2CS_2, $M'_2MC_2S_2$, and $M'_2M_2C_3S_2$; (PDF)

AUTHOR INFORMATION

Corresponding Authors

Haifeng Lv − *National Synchrotron Radiation Laboratory, CAS Center for Excellence in Nanoscience and CAS Key Laboratory for Materials for Energy Conversion, School of Chemistry and Materials Science, CAS Center for Excellence in Nanoscience and Synergetic Innovation of Quantum Information & Quantum Technology, University of Science and Technology of China, Hefei 230029, P. R. China; Zhejiang Institute of Photonelectronics, Jinhua, Zhejiang 321004, P. R. China;* orcid.org/0000-0001-9491-6367; Email: hflv@ustc.edu.cn

Xiaojun Wu − *National Synchrotron Radiation Laboratory, CAS Center for Excellence in Nanoscience and CAS Key Laboratory for Materials for Energy Conversion, School of Chemistry and Materials Science, CAS Center for Excellence in Nanoscience and Synergetic Innovation of Quantum Information & Quantum Technology, University of Science and Technology of China, Hefei 230029, P. R. China; Zhejiang Institute of Photonelectronics, Jinhua, Zhejiang 321004, P. R. China;* orcid.org/0000-0003-3606-1211; Email: xjwu@ustc.edu.cn

Li Song − *National Synchrotron Radiation Laboratory, CAS Center for Excellence in Nanoscience, University of Science and Technology of China, Hefei 230029, P. R. China; Zhejiang Institute of Photonelectronics, Jinhua, Zhejiang 321004, P. R. China;* orcid.org/0000-0003-0585-8519; Email: song2012@ustc.edu.cn

Authors

Hongwei Shou − *National Synchrotron Radiation Laboratory, CAS Center for Excellence in Nanoscience, University of Science and Technology of China, Hefei 230029, P. R. China; CAS Key Laboratory for Materials for Energy Conversion, School of Chemistry and Materials Science, CAS Center for Excellence in Nanoscience and Synergetic Innovation of Quantum Information & Quantum Technology, University of Science and Technology of China, Hefei 230026, P. R. China*

Quan Zhou − *National Synchrotron Radiation Laboratory, CAS Center for Excellence in Nanoscience, University of Science and Technology of China, Hefei 230029, P. R. China*

Shiqiang Wei − *National Synchrotron Radiation Laboratory, CAS Center for Excellence in Nanoscience, University of Science and Technology of China, Hefei 230029, P. R. China*

Hengjie Liu − *National Synchrotron Radiation Laboratory, CAS Center for Excellence in Nanoscience, University of Science and Technology of China, Hefei 230029, P. R. China;* orcid.org/0000-0001-6499-3935

Complete contact information is available at: https://pubs.acs.org/10.1021/jacsau.3c00710

https://doi.org/10.1021/jacsau.3c00710
JACS Au 2024, 4, 930−939

Author Contributions

The computations for this study were designed and executed by Hongwei Shou under the guidance of Quan Zhou, Shiqiang Wei, Hengjie Liu, Li Song, Haifeng Lv, and Xiaojun Wu. All authors contributed to the discussion of the results and provided comments on the manuscript.

Notes

The authors declare no competing financial interest.

■ ACKNOWLEDGMENTS

We acknowledge the financial support from the National Key R&D Program of China (2020YFA0405800 and 2022YFA1504104), NSFC (12225508, U1932201, 22075264, and 12205301), and National Postdoctoral Program for Innovative Talents (BX20230346). H.L. acknowledges the funding from the Fundamental Research Funds for the Central Universities (WK2310000099). The numerical calculations in this paper have been done on the Hefei Advanced Computing Center.

■ REFERENCES

(1) Jiao, S.; Fu, X.; Huang, H. Descriptors for the Evaluation of Electrocatalytic Reactions: d-Band Theory and Beyond. *Adv. Funct. Mater.* **2022**, *32*, 2107651.
(2) Li, W.; Liu, C.; Gu, C.; Choi, J.-H.; Wang, S.; Jiang, J. Interlayer Charge Transfer Regulates Single-Atom Catalytic Activity on Electride/Graphene 2D Heterojunctions. *J. Am. Chem. Soc.* **2023**, *145*, 4774−4783.
(3) Dai, Y.; Li, H.; Wang, C.; Xue, W.; Zhang, M.; Zhao, D.; Xue, J.; Li, J.; Luo, L.; Liu, C.; Li, X.; Cui, P.; Jiang, Q.; Zheng, T.; Gu, S.; Zhang, Y.; Xiao, J.; Xia, C.; Zeng, J. Manipulating local coordination of copper single atom catalyst enables efficient CO2-to-CH4 conversion. *Nat. Commun.* **2023**, *14*, 3382.
(4) Zhang, M.; Ai, X.; Liang, X.; Chen, H.; Zou, X. Key Role of Local Chemistry in Lattice Nitrogen-Participated N2-to-NH3 Electrocatalytic Cycle over Nitrides. *Adv. Funct. Mater.* **2023**, *n/a*, 2306358.
(5) Han, Z.; Zhao, S.; Xiao, J.; Zhong, X.; Sheng, J.; Lv, W.; Zhang, Q.; Zhou, G.; Cheng, H. Engineering d-p Orbital Hybridization in Single-Atom Metal-Embedded Three-Dimensional Electrodes for Li−S Batteries. *Adv. Mater.* **2021**, *33*, 2105947.
(6) Zhou, J.; Liu, X.; Zhu, L.; Zhou, J.; Guan, Y.; Chen, L.; Niu, S.; Cai, J.; Sun, D.; Zhu, Y.; Du, J.; Wang, G.; Qian, Y. Deciphering the Modulation Essence of p Bands in Co-Based Compounds on Li-S Chemistry. *Joule* **2018**, *2*, 2681−2693.
(7) Fang, M.; Han, J.; He, S.; Ren, J.-C.; Li, S.; Liu, W. Effective Screening Descriptor for MXenes to Enhance Sulfur Reduction in Lithium−Sulfur Batteries. *J. Am. Chem. Soc.* **2023**, *145*, 12601−12608.
(8) Fan, K.; Ying, Y.; Lin, Z.; Tsang, Y. H.; Huang, H. Building Up an "Elemental Property-Adsorption Energy Descriptor-Decomposition Barrier" Three-Tier Model for Screening Biatom Catalysts in Sodium-Sulfur Batteries. *Adv. Energy Mater.* **2023**, *13*, 2300871.
(9) Jiao, Y.; Li, H.; Jiao, Y.; Qiao, S.-Z. Activity and Selectivity Roadmap for C−N Electro-Coupling on MXenes. *J. Am. Chem. Soc.* **2023**, *145*, 15572−15580.
(10) Fung, V.; Hu, G.; Ganesh, P.; Sumpter, B. G. Machine learned features from density of states for accurate adsorption energy prediction. *Nat. Commun.* **2021**, *12*, 88.
(11) Isayev, O.; Fourches, D.; Muratov, E. N.; Oses, C.; Rasch, K.; Tropsha, A.; Curtarolo, S. Materials Cartography: Representing and Mining Materials Space Using Structural and Electronic Fingerprints. *Chem. Mater.* **2015**, *27*, 735−743.
(12) Kuban, M.; Rigamonti, S.; Scheidgen, M.; Draxl, C. Density-of-states similarity descriptor for unsupervised learning from materials data. *Sci. Data* **2022**, *9*, 646.
(13) Hammer, B.; Norskov, J. K. Why gold is the noblest of all the metals. *Nature* **1995**, *376*, 238−240.
(14) Tian, X.; Zhao, X.; Su, Y.-Q.; Wang, L.; Wang, H.; Dang, D.; Chi, B.; Liu, H.; Hensen, E. J. M.; Lou, X. W.; Xia, B. Y. Engineering bunched Pt-Ni alloy nanocages for efficient oxygen reduction in practical fuel cells. *Science* **2019**, *366*, 850−856.
(15) Peng, L.; Wei, Z.; Wan, C.; Li, J.; Chen, Z.; Zhu, D.; Baumann, D.; Liu, H.; Allen, C. S.; Xu, X.; Kirkland, A. I.; Shakir, I.; Almutairi, Z.; Tolbert, S.; Dunn, B.; Huang, Y.; Sautet, P.; Duan, X. A fundamental look at electrocatalytic sulfur reduction reaction. *Nat. Catal.* **2020**, *3*, 762−770.
(16) Vojvodic, A.; Nørskov, J. K.; Abild-Pedersen, F. Electronic Structure Effects in Transition Metal Surface Chemistry. *Top. Catal.* **2014**, *57*, 25−32.
(17) Yeo, B. C.; Nam, H.; Nam, H.; Kim, M. C.; Lee, H. W.; Kim, S. C.; Won, S. O.; Kim, D.; Lee, K. Y.; Lee, S. Y.; Han, S. S. High-throughput computational-experimental screening protocol for the discovery of bimetallic catalysts. *npj Comput. Mater.* **2021**, *7*, 137.
(18) Kusada, K.; Yamauchi, M.; Kobayashi, H.; Kitagawa, H.; Kubota, Y. Hydrogen-Storage Properties of Solid-Solution Alloys of Immiscible Neighboring Elements with Pd. *J. Am. Chem. Soc.* **2010**, *132*, 15896−15898.
(19) Yang, A.; Sakata, O.; Kusada, K.; Yayama, T.; Yoshikawa, H.; Ishimoto, T.; Koyama, M.; Kobayashi, H.; Kitagawa, H. The valence band structure of AgxRh1−x alloy nanoparticles. *Appl. Phys. Lett.* **2014**, *105*, 153109.
(20) Hong, D.; Oh, J.; Bang, K.; Kwon, S.; Yun, S.-Y.; Lee, H. M. Interpretable Deep Learning Model for Analyzing the Relationship between the Electronic Structure and Chemisorption Property. *J. Phys. Chem. Lett.* **2022**, *13*, 8628−8634.
(21) Esterhuizen, J. A.; Goldsmith, B. R.; Linic, S. Uncovering electronic and geometric descriptors of chemical activity for metal alloys and oxides using unsupervised machine learning. *Chem. Catalysis* **2021**, *1*, 923−940.
(22) Feng, S.; Fu, Z.; Chen, X.; Li, B.; Peng, H.; Yao, N.; Shen, X.; Yu, L.; Gao, Y.; Zhang, R.; Zhang, Q. An Electrocatalytic Model of the Sulfur Reduction Reaction in Lithium−Sulfur Batteries. *Angew. Chem., Int. Ed.* **2022**, *61*, No. e202211448.
(23) Chen, Z.; Zhao, M.; Hou, L.; Zhang, X.; Li, B.; Huang, J. Toward Practical High-Energy-Density Lithium−Sulfur Pouch Cells: A Review. *Adv. Mater.* **2022**, *34*, 2201555.
(24) Chen, Y.; Wang, T.; Tian, H.; Su, D.; Zhang, Q.; Wang, G. Advances in Lithium-Sulfur Batteries: From Academic Research to Commercial Viability. *Adv. Mater.* **2021**, *33*, 2003666.
(25) Zhou, X.; Cui, Y.; Huang, X.; Wu, X.; Sun, H.; Tang, S. Dual-Defect Engineering of Bidirectional Catalyst for High-Performing Lithium-Sulfur Batteries. *Small* **2023**, 2301545.
(26) Lieu, W. Y.; Lin, C.; Li, X. L.; Jiang, S.; Li, Y.; Yang, H. Y.; Seh, Z. W. Structural Design of Electrocatalyst-Decorated MXenes on Sulfur Spheres for Lithium−Sulfur Batteries. *Nano Lett.* **2023**, *23*, 5762−5769.
(27) Lv, L.; Guo, C.; Sun, W.; Wang, Y. Strong Surface-Bound Sulfur in Carbon Nanotube Bridged Hierarchical Mo2C-Based MXene Nanosheets for Lithium−Sulfur Batteries. *Small* **2019**, *15*, 1804338.
(28) Ding, H.; Li, Y.; Li, M.; Chen, K.; Liang, K.; Chen, G.; Lu, J.; Palisaitis, J.; Persson, P. O. Å.; Eklund, P.; Hultman, L.; Du, S.; Chai, Z.; Gogotsi, Y.; Huang, Q. Chemical scissor−mediated structural editing of layered transition metal carbides. *Science* **2023**, *379*, 1130−1135.
(29) VahidMohammadi, A.; Rosen, J.; Gogotsi, Y. The world of two-dimensional carbides and nitrides (MXenes). *Science* **2021**, *372*, No. eabf1581, DOI: 10.1126/science.abf1581.
(30) Kohn, W.; Sham, L. J. Self-Consistent Equations Including Exchange and Correlation Effects. *Phys. Rev.* **1965**, *140*, A1133−A1138.
(31) Kresse, G.; Furthmüller, J. Efficient iterative schemes for ab initio total-energy calculations using a plane-wave basis set. *Phys. Rev. B* **1996**, *54*, 11169−11186.

https://doi.org/10.1021/jacsau.3c00710
JACS Au 2024, 4, 930−939

(32) Blöchl, P. E. Projector augmented-wave method. *Phys. Rev. B* **1994**, *50*, 17953−17979.
(33) Perdew, J. P.; Burke, K.; Ernzerhof, M. Generalized Gradient Approximation Made Simple. *Phys. Rev. Lett.* **1996**, *77*, 3865−3868.
(34) Grimme, S.; Antony, J.; Ehrlich, S.; Krieg, H. A consistent and accurate ab initio parametrization of density functional dispersion correction (DFT-D) for the 94 elements H-Pu. *J. Chem. Phys.* **2010**, *132*, 154104.
(35) Grimme, S.; Ehrlich, S.; Goerigk, L. Effect of the damping function in dispersion corrected density functional theory. *J. Comput. Chem.* **2011**, *32*, 1456−1465.
(36) Anasori, B.; Lukatskaya, M. R.; Gogotsi, Y. 2D metal carbides and nitrides (MXenes) for energy storage. *Nat. Rev. Mater.* **2017**, *2*, 16098.
(37) Anasori, B.; Xie, Y.; Beidaghi, M.; Lu, J.; Hosler, B. C.; Hultman, L.; Kent, P. R. C.; Gogotsi, Y.; Barsoum, M. W. Two-Dimensional, Ordered, Double Transition Metals Carbides (MXenes). *ACS Nano* **2015**, *9*, 9507−9516.
(38) Houk, K. N. Frontier molecular orbital theory of cycloaddition reactions. *Acc. Chem. Res.* **1975**, *8*, 361−369.
(39) Zhang, J.; Zhao, Y.; Guo, X.; Chen, C.; Dong, C.-L.; Liu, R.-S.; Han, C.-P.; Li, Y.; Gogotsi, Y.; Wang, G. Single platinum atoms immobilized on an MXene as an efficient catalyst for the hydrogen evolution reaction. *Nat. Catal.* **2018**, *1*, 985−992.
(40) Hu, T.; Hu, M.; Gao, B.; Li, W.; Wang, X. Screening Surface Structure of MXenes by High-Throughput Computation and Vibrational Spectroscopic Confirmation. *J. Phys. Chem. C* **2018**, *122*, 18501−18509.
(41) Zhang, P.; Shou, H.; Xia, Y.; Wang, C.; Wei, S.; Xu, W.; Chen, Y.; Liu, Z.; Guo, X.; Zhu, K.; Cao, Y.; Wu, X.; Chen, S.; Song, L. X-ray Insights into Formation of − O Functional Groups on MXenes: Two-Step Dehydrogenation of Adsorbed Water. *Nano Lett.* **2023**, *23*, 1401−1408.
(42) Tan, T. L.; Jin, H. M.; Sullivan, M. B.; Anasori, B.; Gogotsi, Y. High-Throughput Survey of Ordering Configurations in MXene Alloys Across Compositions and Temperatures. *ACS Nano* **2017**, *11*, 4407−4418.
(43) Li, D.; Chen, X.; Xiang, P.; Du, H.; Xiao, B. Chalcogenated-Ti3C2 × 2 MXene (X = O, S, Se and Te) as a high-performance anode material for Li-ion batteries. *Appl. Surf. Sci.* **2020**, *501*, No. 144221.
(44) Zha, X.-H.; Ren, J.-C.; Feng, L.; Bai, X.; Luo, K.; Zhang, Y.; He, J.; Huang, Q.; Francisco, J. S.; Du, S. Bipolar magnetic semiconductors among intermediate states during the conversion from Sc2C(OH)2 to Sc2CO2MXene. *Nanoscale* **2018**, *10*, 8763−8771.
(45) Hong, L.; Klie, R. F.; Öğüt, S. First-principles study of size- and edge-dependent properties of MXene nanoribbons. *Phys. Rev. B* **2016**, *93*, No. 115412.
(46) Wang, L.; Chang, W.-L.; Sun, Z.-Q.; Zhang, Z.-M. Investigations on the thermoelectric and thermodynamic properties of Y2CT2 (T = O, F, OH). *RSC Adv.* **2022**, *12*, 14377−14383.
(47) Zhu, Q.; Xu, H.-F.; Shen, K.; Zhang, Y.-Z.; Li, B.; Yang, S.-B. Efficient polysulfides conversion on Mo2CTx MXene for high-performance lithium−sulfur batteries. *Rare Metals* **2022**, *41*, 311−318.
(48) Wang, Y.; Shen, J.; Xu, L.-C.; Yang, Z.; Li, R.; Liu, R.; Li, X. Sulfur-functionalized vanadium carbide MXene (V2CS2) as a promising anchoring material for lithium−sulfur batteries. *Phys. Chem. Chem. Phys.* **2019**, *21*, 18559−18568.
(49) Wei, C.; Fang, T.; Tang, X.; Wang, P.; Liu, X. Non-Negligible Role of Multifunctional MXene Hosts for Li−S Batteries: Anchoring and Electrocatalysis. *J. Phys. Chem. C* **2022**, *126*, 17066−17075.
(50) Yang, X.; Gao, X.; Sun, Q.; Jand, S. P.; Yu, Y.; Zhao, Y.; Li, X.; Adair, K.; Kuo, L.; Rohrer, J.; Liang, J.; Lin, X.; Banis, M. N.; Hu, Y.; Zhang, H.; Li, X.; Li, R.; Zhang, H.; Kaghazchi, P.; Sham, T.; Sun, X. Promoting the Transformation of Li2S2 to Li2S: Significantly Increasing Utilization of Active Materials for High-Sulfur-Loading Li−S Batteries. *Adv. Mater.* **2019**, *31*, 1901220.
(51) Du, Z.; Chen, X.; Hu, W.; Chuang, C.; Xie, S.; Hu, A.; Yan, W.; Kong, X.; Wu, X.; Ji, H.; Wan, L.-J. Cobalt in Nitrogen-Doped Graphene as Single-Atom Catalyst for High-Sulfur Content Lithium−Sulfur Batteries. *J. Am. Chem. Soc.* **2019**, *141*, 3977−3985.
(52) Wang, R.; Qin, J.; Pei, F.; Li, Z.; Xiao, P.; Huang, Y.; Yuan, L.; Wang, D. Ni Single Atoms on Hollow Nanosheet Assembled Carbon Flowers Optimizing Polysulfides Conversion for Li−S Batteries. *Adv. Funct. Mater.* **2023**, *33*, 2305991.
(53) Zhan, X.; Si, C.; Zhou, J.; Sun, Z. MXene and MXene-based composites: synthesis, properties and environment-related applications. *Nanoscale Horizons* **2020**, *5*, 235−258.
(54) Zhou, B.; Yin, H.; Dong, C.; Sun, L.; Feng, W.; Pu, Y.; Han, X.; Li, X.; Du, D.; Xu, H.; Chen, Y. Biodegradable and Excretable 2D W1.33C i-MXene with Vacancy Ordering for Theory-Oriented Cancer Nanotheranostics in Near-Infrared Biowindow. *Adv. Sci.* **2021**, *8*, 2101043.
(55) Meshkian, R.; Dahlqvist, M.; Lu, J.; Wickman, B.; Halim, J.; Thörnberg, J.; Tao, Q.; Li, S.; Intikhab, S.; Snyder, J.; Barsoum, M. W.; Yildizhan, M.; Palisaitis, J.; Hultman, L.; Persson, P. O. Å.; Rosen, J. W-Based Atomic Laminates and Their 2D Derivative W1.33C MXene with Vacancy Ordering. *Adv. Mater.* **2018**, *30*, 1706409.
(56) Yang, J.; Liu, R.; Jia, N.; Wu, K.; Fu, X.; Wang, Q.; Cui, W. Novel W-based in-plane chemically ordered (W2/3R1/3)2AlC (R = Gd, Tb, Dy, Ho, Er, Tm and Lu) MAX phases and their 2D W1.33C MXene derivatives. *Carbon* **2021**, *183*, 76−83.
(57) Wang, D.; Zhou, C.; Filatov, A. S.; Cho, W.; Lagunas, F.; Wang, M.; Vaikuntanathan, S.; Liu, C.; Klie, R. F.; Talapin, D. V. Direct synthesis and chemical vapor deposition of 2D carbide and nitride MXenes. *Science* **2023**, *379*, 1242−1247.

https://doi.org/10.1021/jacsau.3c00710
JACS Au 2024, 4, 930−939